Substrate Protection with Corrosion Scales: Can we Depend on Iron Carbonate?

Mohammed Al Kindi, Gaurav R. Joshi, Karyn Cooper, Jake Andrews, Paulina Arellanes-Lozada, Rafael Leiva-Garcia, Dirk L Engelberg, Oier Bikondoa, Robert Lindsay

Substrate Protection with Corrosion Scales:

Can we Depend on Iron Carbonate?

Mohammed Al Kindi[1], Gaurav R. Joshi[2], Karyn Cooper[1], Jake Andrews[1], Paulina Arellanes-Lozada[1], Rafael Leiva-Garcia[1], Dirk L. Engelberg[1], Oier Bikondoa[3,4], Robert Lindsay[1,5]

[1]*Corrosion and Protection Centre, Department of Materials, The University of Manchester, Sackville Street, Manchester M13 9PL, UK*

[2]*IFP Energies Nouvelles (Lyon), Rond-point de l'échangeur de Solaize BP-3, 69360 Solaize, France*

[3]*XMaS-ESRF, 71 Av. Des Martyrs, F-38043 Grenoble Cedex, France*

[4]*Department of Physics, University of Warwick, Gibbet Hill Road, Coventry CV4 7AL, UK*

[5]*Photon Science Institute, The University of Manchester, Manchester, M13 9PL, UK.*

Corresponding author Email Address:

robert.lindsay@manchester.ac.uk

Abstract

Controlling corrosion with naturally occurring corrosion scales is potentially a more environmentally sustainable alternative to current approaches, including dosing of organic corrosion inhibitors. We report *operando* grazing incidence X-ray diffractograms correlated with electrochemical measurements to elucidate the growth and corrosion protection properties of a corrosion scale composed of $FeCO_3$ crystallites, which is encountered in various key energy industry applications. Data, acquired as a function of time from high purity iron immersed in CO_2-saturated deionized H_2O at pH = 6.8 and T = 80°C, show that the $FeCO_3$ scale not only prevents corrosion of the covered substrate, but also acts a significant interfacial diffusion barrier for corrosion reagents and/or products once sufficient coverage is achieved. Most notably, from a corrosion engineering perspective, however, it is determined that corrosion, occurring in gaps between scale crystallites, remains appreciable; this important insight is gained through the analysis of electrochemical impedance spectra to estimate the variation in electrochemically active surface area as scale coverage increases. These results indicate that naturally occurring $FeCO_3$ scales are not a tenable solution for corrosion protection, as even in their *intact* state they are highly likely to be, at best, semi-protective.

Keywords: Corrosion, Sweet, Protection, Scale, Iron Carbonate, Operando, Diffraction, Electrochemical

Introduction

Generation of affordable, secure, net-zero energy is possibly the greatest challenge of the age. One issue that plagues this industry is infrastructure degradation through corrosion, which can undermine economic viability, as well as increase the probability of catastrophic failure[1–5]. On this basis, immense effort is being applied to explore routes to control this phenomenon with an increasing emphasis on lower environmental impact solutions[6,7], such as harnessing naturally formed corrosion scales. For instance, it is proposed that the barrier properties of scales formed on carbon steel in aqueous CO_2-saturated (sweet) environments[8–10], encountered in geothermal power plants, carbon capture facilities, and oil production, can mitigate corrosion. Here, we test this hypothesis, providing experimental evidence to suggest that even the protection afforded by *intact* sweet corrosion scales may be undermined by spatially localised corrosion, so that they cannot be relied upon alone for structural integrity.

Sweet corrosion results from the presence of carbonic acid (H_2CO_3(aq)), which is formed through reaction of H_2O with dissolved CO_2. The buffering effect of this aqueous species is reported to underpin the cathodic corrosion reaction (H_2(g) evolution), driving anodic dissolution of the metal atoms (Fe(s) to Fe^{2+}(aq))[11]. Concurrent with substrate dissolution, precipitation of surface adhered siderite ($FeCO_3$) crystallites also often occurs, which has been shown to significantly modify the rate of corrosion[12]. In particular, *operando* studies, where X-ray scattering data are acquired in tandem with electrochemical measurements, have reported that $FeCO_3$ reduces corrosion, offering substantial substrate protection[13–17].

One potential deficiency of the *operando* studies of sweet corrosion scaling[13–17], as well as other *ex situ* work (see, for example, [12]), is the surface area used for calculation of the area-normalised anodic dissolution rate (corrosion rate). It has simply been assumed to be equal to the initial geometric area (G_a) of the sample that is exposed to the solution, and not to vary as a function of immersion time ($t_{immerse}$). In reality, as

illustrated in Figure 1, an increasingly smaller proportion of the surface will be electrochemically active as the electronically insulating $FeCO_3$ scale grows across the substrate, i.e., $S_a(t) < S_a(0)$, where $S_a(t)$ ($S_a(0)$) is the electrochemically active surface area at $t_{immerse}$ = t ($t_{immerse}$ = 0). Consequently, the anodic dissolution rate of the remaining active area may be significantly underestimated in previous *operando* studies, leading one to misjudge the degree of scale-induced protection. In the current study, we examine this topic through combining grazing incidence X-ray diffraction (GIXRD) with electrochemical measurements, i.e., linear polarisation resistance (LPR) and electrochemical impedance spectroscopy (EIS). *Operando* data are acquired as a function of $t_{immerse}$, and an approach applied previously to similar substrate/solution systems[18,19] is employed to determine the fractional $S_a(t)$ from EIS data. Results demonstrate the importance of explicitly considering $S_a(t)$ for evaluating the protection offered by a corrosion scale, raising significant questions about the reliability of siderite as a barrier to corrosion.

Results and Discussion

Figure 2(a) displays a series of GIXRD diffractograms, acquired as a function of immersion time (up to $t_{immerse}$ = 670 min), from a Fe sample submerged in the sweet solution of interest, i.e., pH = 6.80 ± 0.05, T = 80 ± 3°C, $[O_2(aq)] < 20$ ppb, P_{tot} = 1.01 bar, and P_{CO2} = 0.54 bar. The bottommost diffractogram is of a polished substrate, acquired prior to immersion, where the sharp peak at $2\theta \sim 23.4°$ can be attributed to diffraction from {110} planes of α-Fe (ferrite)[12]. Four broader peaks, located at $2\theta \leq 13°$, arise from Kapton components in front of the sample[20]. Sweet solution immersion results in the appearance of a number of other peaks, which initially increase in intensity with time. As indicated by the annotation in Figure 2 (a), all of these peaks can be assigned to $FeCO_3$[12].

Figure 2 (b) provides more quantitative insight into the evolution of the $FeCO_3$ diffraction signal. In this panel, the relative intensity (i.e., integrated peak area) of the

$FeCO_3\{104\}$ diffraction peak ($Int_{rel}(FeCO_3\{104\})$) is plotted versus $t_{immerse}$, where

$$Int_{rel}(FeCO_3\{104\}) = \frac{Int(FeCO_3\{104\})}{Int(Fe\{110\})}. \quad (1)$$

$Int(FeCO_3\{104\})$ and $Int(Fe\{110\})$ are the intensities of the $FeCO_3\{104\}$ and $Fe\{110\}$ diffraction peaks, respectively; the $FeCO_3\{104\}$ diffraction peak was selected as it exhibits the greatest intensity as regards signal from the scale. The data exhibit an approximately sigmoidal increase over the first ~ 300 min of immersion, and then become approximately constant. In the inset in Figure 2 (b), following normalisation such that $Int_{rel}(FeCO_3\{hkl\}) = 1$ at $t_{immerse}$ = 670 min, the $FeCO_3\{104\}$ data are compared to those obtained from the $FeCO_3\{012\}$ and $FeCO_3\{110\}$ diffraction peaks. Evidently, each plot displays a very similar shape, indicating that variation in preferential orientation of the crystalline sweet corrosion scale does not impact significantly on the observed profiles[16].

Based on results presented in Ref.[12], the profile of $Int_{rel}(FeCO_3\{104\})$ in Figure 2 (b) is expected to correspond to a decrease in corrosion rate. To verify this assertion, mimicking earlier *operando* studies[16,20], the corrosion rate ($CR_{(LPR)}$) as a function of immersion time has been determined from the polarisation resistance of the interface ($R_{P(LPR)}$) obtained from concurrent LPR measurements[21]. For these calculations, a Stern-Geary coefficient (B) of 38 mV/decade[12], along with a sample area (G_a) of 0.785 cm^2, were employed, and the solution resistance ($R_{s(EIS)}$), estimated from EIS data, was removed; Table S1 in Supporting Information lists the relevant equations and calculated data. The resulting $CR_{(LPR)}$ values are plotted in Figure 3, together with $Int_{rel}(FeCO_3\{104\})$, as a function of $t_{immerse}$. The $CR_{(LPR)}$ and $Int_{rel}(FeCO_3\{104\})$ profiles more or less inversely mirror each other, suggesting that, under the current experimental conditions, there is a linear relationship between sweet corrosion rate and fractional coverage of $FeCO_3$, i.e.,

$$CR_{(LPR)}=CR^{0}_{(LPR)}(1-\theta_{scale}). \quad (2)$$

$CR^{0}_{(LPR)}$ is the corrosion rate in the absence of scale, and θ_{scale} is the fractional surface coverage of scale, where θ_{scale} = 1 corresponds to complete coverage of the substrate, i.e., the aqueous solution cannot contact the iron substrate at θ_{scale} = 1.

To test the applicability of Equation 2 to the current experiment, namely that there is linear relationship between corrosion rate and scale coverage, we posit that $Int_{rel}(FeCO_3\{104\})$ is directly proportional to θ_{scale}. Clearly, this assumption is not necessarily valid, as $Int_{rel}(FeCO_3\{104\})$ is a measure of scale volume rather than lateral coverage. Scanning electron microscopy (SEM) images presented in Ref.[12], including scale/substrate cross-sections acquired using focused ion beam (FIB) SEM, however, support such a correspondence. They demonstrate that the growth mode of the scale layer on high purity iron is predominantly lateral under similar conditions, i.e., there is no significant variation in the depth of adhered scale as θ_{scale} increases; the scale is always composed of a single layer of $FeCO_3$ crystallites, which have a mean size in the range ~ 5 – 15 μm[12]. On this basis, $CR_{(LPR)}$ and $Int_{rel}(FeCO_3\{104\})$ are plotted against each other in the inset in Figure 3; interpolation has been undertaken to generate $Int_{rel}(FeCO_3\{104\})$ datapoints that match $CR_{(LPR)}$ in terms of $t_{immerse}$. A straight line fit to these data is also shown (dashed line), suggesting that $CR_{(LPR)}$ and $Int_{rel}(FeCO_3\{104\})$ are approximately linearly related, and so Equation 2 appears to be a reasonable descriptor of the dependence of corrosion rate on scale coverage. This relationship is similar to that concluded in previous *operando* GIXRD work, albeit several studies indicate a delay between the appearance of crystalline $FeCO_3$ and the onset of substrate protection[15–17]; the origin of this discrepancy may be related to experimental details, such as the employment of carbon steel as a substrate in the earlier work, rather than the high purity iron used here.

Focusing on the corrosion rate in Figure 3, it is reduced by ~ 95% (~ 0.80 mm y^{-1} to ~ 0.05 mm y^{-1}), suggesting that the scale is providing substantial corrosion protection.

This deduction may be misleading, however, as we have, yet, not considered any reduction in the electrochemically active surface area (S_a), resulting from the presence of electrochemically inert (electronically insulating) $FeCO_3$ scale, as illustrated in Figure 1. To address this issue the *relative* electrochemically active surface area (S_a^{rel}) can be estimated using the following[18,19]:

$$S_a^{rel} = \frac{S_a(t)}{S_a(0)} = \frac{C_{dl}(t)}{C_{dl}(0)}. \quad (3)$$

$C_{dl}(t)$ and $C_{dl}(0)$ are the effective double layer capacitances at $t_{immerse}$ = t min and $t_{immerse}$ = 0 min, respectively, which can be estimated from the EIS data that were acquired along with the LPR measurements,.

The common approach of using an equivalent electrical circuit (EEC) to represent the pertinent interfacial processes throughout the immersion period has been adopted to analyse the EIS data[21]. Having explored several options, the circuit displayed in Figure 4 (a) was found to be the most appropriate, capable of satisfactorily fitting the experimental impedance data, whilst also representing the underlying physicochemical processes. It comprises the following components: two ohmic resistors, labelled $\mathbf{R_s}$ and $\mathbf{R_{ct}}$, to account for solution resistance ($R_{s(EIS)}$) and charge transfer resistance ($R_{ct(EIS)}$), respectively; a constant phase element, $\mathbf{Q_{dl}}$, to describe the capacitive-like nature of the electrode/solution interface; and a finite length Warburg impedance element, $\mathbf{W_d}$, to quantify limited diffusion (mass transport) across the surface scale.

Best fits (dashed lines) to selected EIS data (Nyquist plots), using the EEC in Figure 4 (a), are shown in Figure 4 (b). Table S2 in Supporting Information lists the corresponding best fit parameters, along with the number of optimised parameters and the goodness of fit (χ^2). Using these data, C_{dl}, and subsequently S_a^{rel}, have been determined for each $t_{immerse}$, applying a relationship developed by Brug *et al.*[22]; the output of these calculations is compiled in Table S3.

Plots of $Int_{rel}(FeCO_3\{104\})$ and S_a^{rel} as a function of $t_{immerse}$ are compared in Figure 5 (a). The profiles are consistent with electrochemically inert $FeCO_3$ scale blocking anodic/cathodic sites, i.e., $Int_{rel}(FeCO_3\{104\})$ (S_a^{rel}) increases (decreases) until $t_{immerse}$ ~ 300 min and then becomes constant. S_a^{rel} is reduced by a factor of approximately four over the period of substrate immersion. The impact of this variation on calculated corrosion rate is illustrated in Figure 5 (b), which shows the temporal evolution of corrosion rate determined from LPR measurements both with ($CR_{(LPR)}^{S_a corr}$) and without ($CR_{(LPR)}$) correction for S_a^{rel}. Clear differences are apparent, indicating the importance of considering S_a^{rel} for assessing the protection offered by electrochemically inert corrosion scale. Most notably, $CR_{(LPR)}^{S_a corr}$ stabilises at a value of ~ 0.2 mm y^{-1}, which is almost half an order of magnitude greater that the uncorrected corrosion rate ($CR_{(LPR)}$ ~ 0.05 mm y^{-1}). Furthermore, in contrast to the $CR_{(LPR)}$ data, $CR_{(LPR)}^{S_a corr}$ exhibits a peak at $t_{immerse}$ ~ 120 min. A previous *operando* study[17], where measurements were made with the sample anodically polarised, has attributed a similar peak in current density to *direct electrochemical formation* of $FeCO_3$, as the peak maximum coincides with the highest scale growth rate. Here, as indicated by the vertical dashed grey line superimposed on Figure 5, the $CR_{(LPR)}^{S_a corr}$ peak maximum ($t_{immerse}$ ~ 120 min) occurs somewhat prior to the maximum in scale growth kinetics at $t_{immerse}$ ~ 220 min, as determined from the gradient of the $Int_{rel}(FeCO_3\{104\})$ plot. This observation suggests another source for the peak at $t_{immerse}$ ~ 120 min in the current case, such as local variation in interfacial chemistry (e.g., pH) as scale grows.

Besides the initial peak, one other point that is raised by the $CR_{(LPR)}^{S_a corr}$ profile in Figure 5 (b) is the origin of the overall reduction in corrosion rate with increasing scale coverage. Given that the data have been normalised with respect to the relative electrochemical area (S_a^{rel}), then one might suppose that the corrosion rate would display similar values at both $t_{immerse}$ = 0 min and $t_{immerse}$ = 660 min; this assumption is

implicit in the relationship expressed in Equation 2, i.e., $CR_{(LPR)}$ is proportional to the area not covered by $FeCO_3$ scale. A possible explanation of this apparent discrepancy is that the scale permeability is reduced as it evolves, restricting diffusion of reactants/products to/from the corroding surface, and so impeding corrosion kinetics. To test this proposal, the scale's diffusion resistance, $R_{\delta(EIS)}$, has been estimated from the two parameters, Y_{W_d} and B (see Table S2), obtained from fitting of the finite length Warburg impedance element, $\mathbf{W_d}$**;** calculated $R_{\delta(EIS)}$ values, along with those obtained following correction for S_a^{rel} ($R_{\delta(EIS)}^{S_a corr}$), are listed in Table S4.

Figure 6 (a), in which both $R_{\delta(EIS)}^{S_a corr}$ and $Int_{rel}(FeCO_3\{104\})$ are plotted versus $t_{immerse}$, shows that once there is an appreciable amount of surface scale, $R_{\delta(EIS)}^{S_a corr}$ starts to increase similarly to $Int_{rel}(FeCO_3\{104\})$. This observation indicates that as scale coverage increases it does not simply block covered substrate, but also impedes access of aqueous species to/from the remaining electrochemically active surface. Such a decrease in scale permeability explains, at least partially, why the $CR_{(LPR)}^{S_a corr}$ profile (see Figure 5 (b)) shows an overall reduction with immersion time. It should be noted that the S_a^{rel}corrected charge transfer resistance, $R_{ct(EIS)}^{S_a corr}$, plotted as a function of $t_{immerse}$ along with $Int_{rel}(FeCO_3\{104\})$ in Figure 6 (b), exhibits a similar increase with immersion time. This trend suggests that the reduction in scale permeability not only impedes reactant/product flow, but also results in more benign local chemistry, contributing to the lower corrosion rate ($CR_{(LPR)}^{S_a corr}$) at $t_{immerse}$ = 660 min.

To illustrate our interpretation of the *operando* GIXRD/EIS measurements, a cartoon of the evolution of the iron/sweet solution interface as a function of immersion time is presented in Figure 7. Moving from left to right, as scale coverage increases, the relative electrochemically active surface area (S_a^{rel}) decreases; $FeCO_3$, assumed to be electrochemically inert (electrically insulating), is not able to support anode/cathode chemistry. Once the scale coverage becomes significant, it begins to impede the flow (yellow arrows) of corrosion reagents/products to/from the iron surface, as depicted in

the panel to the right by the reduced width of the yellow arrows. Moreover, we suggest that the interfacial solution corrosivity also varies with immersion time, becoming initially more aggressive and then more benign; this phenomenon is indicated by the variation in solution colour at the interface.

Focusing on the loss of electrochemically active surface area, resulting from scale growth, we have demonstrated here that this can have a significant impact on corrosivity assessment. It was determined that at $t_{immerse}$ = 660 min, where the corrosion processes had apparently achieved a steady state, the local substrate penetration (corrosion) rate was underestimated by a factor of approximately four, i.e., ~ 0.2 mm y^{-1} versus ~ 0.05 mm y^{-1}. Such a difference would almost certainly have implications for corrosion management strategy in industrial scenarios, as failure due to local loss of structural integrity becomes a concern. Moreover, this finding suggests that the use of LPR probes[23], which are widely used by corrosion engineers for practical corrosion monitoring, may need to be reconsidered if significant scaling is likely. It should be stressed that the issue of loss of electrochemically active surface could also be an issue where non-corrosion electrochemically inert scales (e.g., $CaCO_3$) are formed[18], and so needs to be borne in mind in such scenarios.

Finally, it is interesting to compare the protection provided by $FeCO_3$ corrosion scale to that afforded through the addition of organic surface actives, namely corrosion inhibitors[6,24]; the latter are a well-established corrosion control approach. These species reduce corrosion through binding to the corroding substrate, typically forming a monolayer/bilayer[24]. On that basis, one could presume that localised corrosion may also be an issue if corrosion inhibitor coverage of the substrate is incomplete, as is typically the case. A key difference, however, is that there is a dynamic equilibrium between adsorbed corrosion inhibitor species and those in bulk solution. Hence, the lateral location of any gaps in the adsorbed layer will vary with time, averaging out

corrosion over the entire exposed surface, i.e., it is appropriate to use initial geometric area (G_a) to estimate corrosion rate.

In sharp contrast to adsorbed corrosion inhibitors, there is no evidence to date suggesting that $FeCO_3$ scales, once established, are appreciably dynamic. Consequently, localised corrosion is an omnipresent concern. To overcome this impediment to utilising $FeCO_3$ scales as an effective corrosion control measure, engineering intervention is required. For example, one could seek to enhance their dynamic nature by periodically conducting cycles of dissolution/reprecipitation through chemical treatment. Alternatively, chemical additives could be employed to further reduce the permeability of the scale, increasing $R_{\delta(EIS)}^{S_a corr}$, and so minimse the corrosion rate of the remaining electrochemically active surface. Some effort has already been applied to enhancing the protective properties of $FeCO_3$[25], but further work is required to develop reliable and sustainable solutions. In addition, when *in situ* chemical intervention is not possible, surface pre-treatment prior to service to enhance and retain formed corrosion scales, such as functionally grading the surface by modifying its metallurgy/composition, could be envisaged.

Conclusion

In summary, through combined *operando* GIXRD/LPR/EIS measurements, the temporal evolution of the growth and corrosion control properties of a $FeCO_3$ scale formed on high purity iron in sweet solution has been elucidated. It is demonstrated that the $FeCO_3$ scale does not simply block corrosion of covered substrate, but also impedes corrosion in the gaps between scale crystallites once sufficient coverage is achieved. Moreover, estimation of the relative electrochemically active surface area with electrochemical impedance spectroscopy has enabled more robust calculation of localised corrosion rates, demonstrating that such scales are less protective than often perceived previously. These results have key implications for the use of naturally occurring $FeCO_3$, and other surface scales, as a barrier to corrosion. In our opinion,

even in their *intact* state (i.e., ignoring local physical/chemical breakdown), these scales are highly likely to be, at best, semi-protective, and *in situ* chemical treatment and/or surface pre-treatment is required to guarantee their reliability.

Methods

High purity Fe rod (10 mm diameter; Purity: 99.99+%; Supplier: Goodfellow) was used as the source material for samples in this study; Table S5 in Supporting Information lists typical impurities. Initially, this rod was annealed (~ 950°C) and cooled in an argon furnace to produce a well-defined microstructure[26], as shown in Figure S1. Subsequently, disc samples (~ 4 mm in depth) were cut from the rod, and ground with a series of SiC papers (240 grit, 600 grit, 1200 grit, 2400 grit, and 4000 grit). Each one was spot welded to a Ni-Cr wire to facilitate electrochemical measurement and stored in a desiccator. Immediately prior to employing one of these samples, it was once again ground with 4000 grit SiC paper, washed with ethanol, and dried under a flow of nitrogen gas (N.B. On the basis of previous work (e.g. Ref.[27]), we expect such a sample to be terminated by a several nanometer thick layer of oxidic iron, along with a topmost film of adventitious carbon.).

Diffraction measurements from these samples were performed employing synchrotron radiation (SR) from beam line BM28 (XMaS) at the European Synchrotron Radiation Facility (ESRF) in Grenoble, France[28]. A photon energy of $h\nu$ = 14.5 keV and an incidence angle (α_i) of 3° were used for data acquisition. Scattered X-rays were recorded with a Dectris 300K-W Pilatus 2D detector, which was able to capture the entire scattering angle (2θ) range of interest in one snapshot. This detector was located at a distance of ~ 320 mm from the sample, such that its surface normal subtended an angle of 18° with respect to the SR beam direction.

To facilitate *in situ* GIXRD measurements, a custom-built electrochemical cell (E-cell) was mounted on BM28. This cell, depicted in Figure S2(a), is a modified version of one employed previously by our group[20], upgraded to allow more precise control of sample height, as well as further minimise O_2 ingress; more details of this E-cell are provided in Supporting Information. Concerning the Fe sample (working electrode), this was secured with glue (Loctite Superglue) onto the polyvinylidene (PVDF) sample post to expose one flat surface of the disc (area ~ 0.785 cm^2) to the sweet solution; the circular edge of the disc was painted with lacomit varnish.

Figure S2(b) shows a schematic diagram of the experimental setup associated with the E-cell to ensure that high quality diffraction data could be acquired under the desired experimental conditions. A rigorous preparation procedure was undertaken to ensure that the required solution chemistry was achieved, including minimising [O_2(aq)]. Initially, deionised H_2O was purged with high purity CO_2 (99.995 %) in a 1 L glass bottle for ~ 2 h (not shown in Figure 2(b)). Subsequently, the solution was heated to T = 80 ± 1°C, and the pH adjusted to 6.80 ± 0.05 with $NaHCO_3$ (Analytical Reagent Grade, Fischer Scientific). Next, the solution was transferred to a 0.6 L Hastelloy autoclave (Parr Instrument), where it was purged with CO_2 gas (*Cylinder 1* in Figure 2(b)) at T = 80 ± 1°C for a further 28 hours. At the end of this period, the [O_2(aq)] was found to be < 20 ppb, as measured by an electrochemical oxygen sensor in the *O_2 Measurement Loop* (Orbisphere A1100, Hach Lang). Concurrently, CO_2 from *Cylinder 2* was used to purge the E-cell and associated lines to prevent O_2(g) dissolution during solution transfer. In addition, as depicted in Figure 2(b) (*Heating Loop*), a hot (~ 95°C) aqueous Na_2SO_3 solution was flowed through the coiled PTFE heat-exchanger tubing in the E-cell to ensure a temperature of ~ 80°C was maintained upon solution transfer

from autoclave to E-cell. The Na_2SO_3 (~ 10 g) served as an O_2 scavenger to avoid O_2 diffusion through the PTFE heat-exchanger tubing.

Having fully prepared the sweet solution in the autoclave vessel (pH = 6.80 ± 0.05, T = 80 ± 1°C, $[O_2(aq)]$ < 20 ppb), ~ 350 ml was transferred to the E-cell. Once filling was complete, the immersion period of the Fe sample was considered to commence (i.e. $t_{immerse}$ = 0 min), and electrochemical measurements were initiated. More specifically, LPR (scan range ± 10 mV vs. open circuit potential, scan rate $1 mVs^{-1}$) and EIS (6 kHz – 100 mHz, ± 10 mV peak voltage) data were regularly acquired, using an Interface 1000 (Gamry Instruments) potentiostat. The sample was maintained at OCP in between LPR and EIS measurements.

Alongside undertaking LPR/EIS, *in situ* GIXRD data were recorded for period of ~ 1 min each 30 min, starting at $t_{immerse}$ = 50 min; the sample was only exposed to X-rays during this time. For these measurements, the Kapton film above the sample was deflated, using a peristaltic pump to remove solution from the E-cell, to achieve a so-called thin-film geometry; this geometry reduces attenuation of the X-rays due to solution scattering. Following acquisition of the 2D diffraction pattern, the Kapton film was re-inflated to return to a thick-film geometry to ensure that corrosion chemistry is not impeded. Figure S4 shows cartoons of these two measurement geometries.

LPR/EIS and *in situ* GIXRD data were recorded with the sample at T = 80 ± 3°C for a total of 660 min. At $t_{immerse}$ = 660 min, the vertical position of the sample was temporarily shifted by ~ 1 mm to acquire a diffraction pattern from another sample location to assess the influence of X-ray exposure on the data. No significant variation

in signal was observed.

Concerning data analysis, following initial assessment of the 2D GIXRD patterns, they were converted to 1D diffractograms for further analysis, i.e., plots of scattered X-ray intensity versus 2θ. The esaProject software package[29] was used for this purpose, which enables collection geometry corrections, diffraction ring integration, and removal of background/glitches. Peak assignment was undertaken using the International Centre for Diffraction Database as a reference[30]. EIS data were fitted using EEC components to extract pertinent parameters, using Electrochemical Impedance Spectroscopy Software (Gamry Instruments).

Supporting Information

Text document with tables and equations pertinent to analysis of electrochemical data, sample composition and microstructure, and details of E-cell.

Acknowledgements

Funding and technical support from bp through the bp International Centre for Advanced Materials (bp-ICAM) and EPSRC through the prosperity partnership (EP/G036850/1) is acknowledged. More particularly, we are grateful to Silvia Vargas and Ming Wei, bp mentors, for their insightful comments. MAK thanks the Petroleum Development Oman for funding of his PhD studentship. We also thank David Chorlton for his invaluable input into designing the E-cell. The GIXRD measurements were undertaken on the EPSRC-funded *XMaS* beamline at the ESRF, directed by M.J. Cooper, C.A. Lucas and T.P.A. Hase.

Data Availability

Data presented in this paper are available to download from Mendeley Data at https://data.mendeley.com/datasets/zygydwry9v/1.

References

(1) Koch, G.; Varney, J.; Thompson, N.; Moghissi, O.; Gould. M.; Payer, J. *NACE 2016 Impact Study, International Measures of Prevention Application, and Economics of Corrosion Technologies Study*, 2016.

(2) Barker, R.; Hua, Y.; Neville, A. Internal Corrosion of Carbon Steel Pipelines for Dense-Phase CO_2 Transport in Carbon Capture and Storage (CCS) – A Review. *Int. Mater. Rev.* **2017**, *62* (1), 1–31.

(3) Mobaraki Nejad, A. A Review of Contributing Parameters in Corrosion of Oil and Gas Wells. *Anti-Corros. Method M.* **2018**, *65* (1), 73–78.

(4) Nogara, J.; Zarrouk, S. J. Corrosion in Geothermal Environment: Part 1: Fluids and Their Impact. *Renew. Sust. Energ. Rev.* **2018**, *82*, 1333–1346.

(5) Nogara, J.; Zarrouk, S. J. Corrosion in Geothermal Environment Part 2: Metals and Alloys. *Renew. Sust. Energ. Rev.* **2018**, *82*, 1347–1363.

(6) Sharma, S.; Kumar, A. Recent Advances in Metallic Corrosion Inhibition: A Review. *J. Mol. Liq.* **2021**, *322*, 114862.

(7) Chauhan, D. S.; Quraishi, M. A.; Qurashi, A. Recent Trends in Environmentally Sustainable Sweet Corrosion Inhibitors. *J. Mol. Liq.* **2021**, *326*, 115117.

(8) Barker, R.; Burkle, D.; Charpentier, T.; Thompson, H.; Neville, A. A Review of Iron Carbonate ($FeCO_3$) Formation in the Oil and Gas Industry. *Corros. Sci.* **2018**, *142*, 312–341.

(9) Ahmad, E. A.; Chang, H.-Y.; Al-Kindi, M.; Joshi, G. R.; Cooper, K.; Lindsay, R.; Harrison, N. M. Corrosion Protection through Naturally Occurring Films: New Insights from Iron Carbonate. *ACS Appl. Mater. Interfaces* **2019**, *11* (36), 33435–33441.

(10) Fioravante, I.; Nunes, R.; Acciari, H.; Codaro, E. Films Formed on Carbon Steel in Sweet Environments - A Review. *J. Braz. Chem. Soc.* **2019**, *30* (7), 1341-1349.

(11) Kahyarian, A.; Brown, B.; Nešić, S. The Unified Mechanism of Corrosion in Aqueous Weak Acids Solutions: A Review of the Recent Developments in

Mechanistic Understandings of Mild Steel Corrosion in the Presence of Carboxylic Acids, Carbon Dioxide, and Hydrogen Sulfide. *Corrosion* **2020**, *76* (3), 268–278.

(12) Joshi, G. R.; Cooper, K.; Zhong, X.; Cook, A. B.; Ahmad, E. A.; Harrison, N. M.; Engelberg, D. L.; Lindsay, R. Temporal Evolution of Sweet Oilfield Corrosion Scale: Phases, Morphologies, Habits, and Protection. *Corros. Sci.* **2018**, *142*, 110–118.

(13) Ingham, B.; Ko, M.; Kear, G.; Kappen, P.; Laycock, N.; Kimpton, J. A.; Williams, D. E. In Situ Synchrotron X-Ray Diffraction Study of Surface Scale Formation during CO_2 Corrosion of Carbon Steel at Temperatures up to 90°C. *Corros. Sci.* **2010**, *52* (9), 3052–3061.

(14) Ingham, B.; Ko, M.; Laycock, N.; Burnell, J.; Kappen, P.; Kimpton, J. A.; Williams, D. E. In Situ Synchrotron X-Ray Diffraction Study of Scale Formation during CO_2 Corrosion of Carbon Steel in Sodium and Magnesium Chloride Solutions. *Corros. Sci.* **2012**, *56*, 96–104.

(15) Ingham, B.; Ko, M.; Laycock, N.; Kirby, N. M.; Williams, D. E. First Stages of Siderite Crystallisation during CO_2 Corrosion of Steel Evaluated Using in Situ Synchrotron Small- and Wide-Angle X-Ray Scattering. *Faraday Discuss.* **2015**, *180*, 171–190.

(16) Burkle, D.; De Motte, R.; Taleb, W.; Kleppe, A.; Comyn, T.; Vargas, S. M.; Neville, A.; Barker, R. In Situ SR-XRD Study of $FeCO_3$ Precipitation Kinetics onto Carbon Steel in CO_2-Containing Environments: The Influence of Brine pH. *Electrochim. Acta* **2017**, *255*, 127–144.

(17) Sk, M. H.; Abdullah, A. M.; Ko, M.; Ingham, B.; Laycock, N.; Arul, R.; Williams, David. E. Local Supersaturation and the Growth of Protective Scales during CO_2 Corrosion of Steel: Effect of pH and Solution Flow. *Corros. Sci.* **2017**, *126*, 26–36.

(18) Devos, O.; Gabrielli, C.; Tribollet, B. Simultaneous EIS and *In Situ* Microscope Observation on a Partially Blocked Electrode Application to Scale Electrodeposition. *Electrochim. Acta* **2006**, *51* (8–9), 1413–1422.

(19) De Motte, R.; Basilico, E.; Mingant, R.; Kittel, J.; Ropital, F.; Combrade, P.; Necib, S.; Deydier, V.; Crusset, D.; Marcelin, S. A Study by Electrochemical Impedance Spectroscopy and Surface Analysis of Corrosion Product Layers Formed during CO_2 Corrosion of Low Alloy Steel. *Corros. Sci.* **2020**, *172*, 108666.

(20) Joshi, G. R.; Cooper, K.; Lapinski, J.; Engelberg, D. L.; Bikondoa, O.; Dowsett M. G.; Lindsay R. In Situ Grazing Incidence X-ray Diffraction of Sweet Corrosion Scaling on Carbon Steel. *CORROSION 2015*, NACE International (2015), Paper Number 5674.

(21) Cottis, R.A. Electrochemical Methods. In *Shreir's Corrosion,* Elsevier, 2010; pp. 1341–1373.

(22) Brug, G.J.; Van Den Eeden, A.L.G.; Sluyters-Rehbach, M., Sluyters J.H. The Analysis of Electrode Impedances Complicated by the Presence of a Constant Phase Element. J. Electroanal. Chem. **1984**, *176*, 275-295.

(23) Wu, J.-W.; Bai, D.; Baker, A. P.; Li, Z.-H.; Liu, X.-B. Electrochemical Techniques Correlation Study of On-Line Corrosion Monitoring Probes: Electrochemical Techniques Correlation Study. *Mater. and Corros.* **2015**, *66* (2), 143–151.

(24) Lindsay, R.; Lyon, S. B. Introduction to Control of Corrosion by Environmental Modification. In *Shreir's Corrosion*; Elsevier, 2010; pp 2891–2899.

(25) Taleb, W.; Pessu, F.; Wang, C.; Charpentier, T.; Barker, R.; Neville, A. Siderite Micro-Modification for Enhanced Corrosion Protection. *npj Mater Degrad* **2017**, *1* (1), 13.

(26) Digges, T.G.; Rosenberg, S.J.; Geil, G.W. *Heat Treatment and Properties of Iron and Steel*. NBS Monograph, Gaithersburg MD, 1966.

(27) Kousar, K.; Walczak, M. S.; Ljungdahl, T.; Wetzel, A.; Oskarsson, H.; Restuccia, P.; Ahmad, E. A.; Harrison, N. M.; Lindsay, R. Corrosion inhibition of carbon steel in hydrochloric acid: Elucdiating the performance of an imidazoline-based surfactant. *Corros. Sci.* 2021, *180*, 109195.

(28) Brown, S. D.; Bouchenoire, L.; Bowyer, D.; Kervin, J.; Laundy, D.; Longfield, M. J.; Mannix, D.; Paul, D. F.; Stunault, A.; Thompson, P.; Cooper, M. J.; Lucas, C. A.; Stirling, W. G. The XMaS Beamline at ESRF: Instrumental Developments and High-Resolution Diffraction Studies. *J Synchrotron Radiat.* **2001**, *8* (6), 1172–1181.

(29) Dowsett. M. G.; Adriaens, A. *esaProject.* See https://warwick.ac.uk/fac /cross_fac/xmas/other_projects/esaproject/. (Last accessed: August 2021).

(30) Gates-Rector, S.; Blanton, T. The Powder Diffraction File: A Quality Materials Characterization Database. *Powder Diffr.* **2019**, 34 (4), 352–360.

(31) Mercier-Bion, F.; Li, J.; Lotz, H.; Tortech, L.; Neff, D.; Dillmann, P. Electrical Properties of Iron Corrosion Layers Formed in Anoxic Environments at the Nanometer Scale. *Corros. Sci.* **2018**, *137*, 98–110.

Figure Captions

Figure 1. Cartoon illustrating loss of electrochemically active surface area (Sa) as a function of increasing $FeCO_3$ scale coverage. At $t_{immerse}$ = 0, the electrochemically active surface area (Sa(0)) is equal to the initial geometric area (G_a) of the carbon steel sample that is exposed to the solution. Consistent with previous work[31], the $FeCO_3$ scale is assumed to be electrochemically inert, i.e., anodic/cathodic reactions do not occur at the surface of this phase.

Figure 2. (a) A series of diffractograms, acquired as a function of immersion time, from a Fe sample submerged in a sweet solution at pH = 6.80 ± 0.05, T = 80 ± 3°C, and [O_2(aq)] < 20 ppb. The bottommost diffractogram is of a polished substrate, acquired prior to immersion. Diffraction peaks are labelled. (b) A plot of the relative intensity of the $FeCO_3${104} diffraction peak ($Int_{rel}(FeCO_3\{104\})$) as a function of $t_{immerse}$. The inset compares normalised $Int_{rel}(FeCO_3\{hkl\}$ versus $t_{immerse}$ profiles for {104} (red circles), {012} (green triangles) and {110} (blue squares) diffraction peaks; these profiles have been normalised to have an intensity of 1 at $t_{immerse}$ = 670 min.

Figure 3. Plots of $Int_{rel}(FeCO_3\{104\})$ (red circles, lefthand y-axis) and $CR_{(LPR)}$ (blue diamonds, righthand y-axis) as a function of $t_{immerse,}$ acquired from a Fe sample submerged in a sweet solution (pH = 6.80 ± 0.05, T = 80 ± 3°C, and [O_2(aq)] < 20 ppb). Inset shows plot of $CR_{(LPR)}$ versus $Int_{rel}(FeCO_3\{104\})$; dashed line is a straight line best fit to these data.

Figure 4. (a) EEC used for fitting of experimental EIS data.. $\mathbf{R_s}$ and $\mathbf{R_{ct}}$ are ohmic resistors, describing solution resistance ($R_{s(EIS)}$) and charge transfer resistance ($R_{ct(EIS)}$), respectively. $\mathbf{Q_{dl}}$ is a constant phase element, that takes account of the capacitive-like nature of the electrode/solution. $\mathbf{W_d}$ is a finite length Warburg impedance, used to describe limited diffusion (mass transport) through surface scale. (b) Selected EIS data (Nyquist plots), showing the evolution of the signal from $t_{immerse}$ = 60 min to $t_{immerse}$ = 660 min. The best fit (dashed line) to each experimental profile, using the EEC displayed in (a), is also shown. Annotation indicates the specific frequencies that correspond to particular impedance data points.

Figure 5. (a) Plots of $Int_{rel}(FeCO_3\{104\})$ (red circles, lefthand y-axis) and S_a^{rel} (blue diamonds, righthand y-axis) as a function of $t_{immerse}$, acquired from a Fe sample submerged in a sweet solution (pH = 6.80 ± 0.05, T = 80 ± 3°C, and $[O_2(aq)] < 20$ ppb). (b) Plots of $CR_{(LPR)}^{S_a corr}$ (red circles) and $CR_{(LPR)}$ (blue diamonds) as a function of $t_{immerse}$. The vertical dashed grey line indicates the maximum in the $CR_{(LPR)}^{S_a corr}$ profile.

Figure 6. (a) Plots of $Int_{rel}(FeCO_3\{104\})$ (red circles, lefthand y-axis) and $R_{\delta(EIS)}^{S_a corr}$ (blue diamonds, righthand y-axis) as a function of $t_{immerse}$. (b) Plots of $Int_{rel}(FeCO_3\{104\})$ (red circles, lefthand y-axis) and $R_{ct(EIS)}^{S_a corr}$ (green squares, offset righthand y-axis) as a function of $t_{immerse}$. Data were acquired from a Fe sample submerged in a sweet solution (pH = 6.80 ± 0.05, T = 80 ± 3°C, and $[O_2(aq)] < 20$ ppb).

Figure 7 Cartoon, derived from *operando* GIXRD/EIS data, depicting the evolution of the iron/sweet solution interface as a function of immersion time ($t_{immerse}$); data were acquired from a Fe sample submerged in a sweet solution (pH = 6.80 ± 0.05, T = 80 ± 3°C, and $[O_2(aq)] < 20$ ppb). S_a^{rel} indicates, the relative electrochemically active surface area. Yellow

arrows denote the flow of corrosion reagents (i.e., H_2CO_3*, with the asterisk indicating that the reagent is either molecular H_2CO_3(aq), CO_2(aq) or some related species, e.g. HCO_3^-(aq)) and products (i.e., Fe^{2+} and H_2) to/from the iron surface. The reduced width of the yellow arrows in the panel to the right indicate that the scale is impeding flow of the reagent/products. Variation in interfacial solution corrosivity is indicated by the variation in solution colour at the interface.

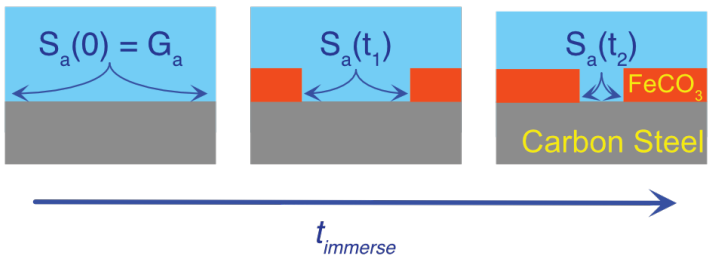

Figure 1

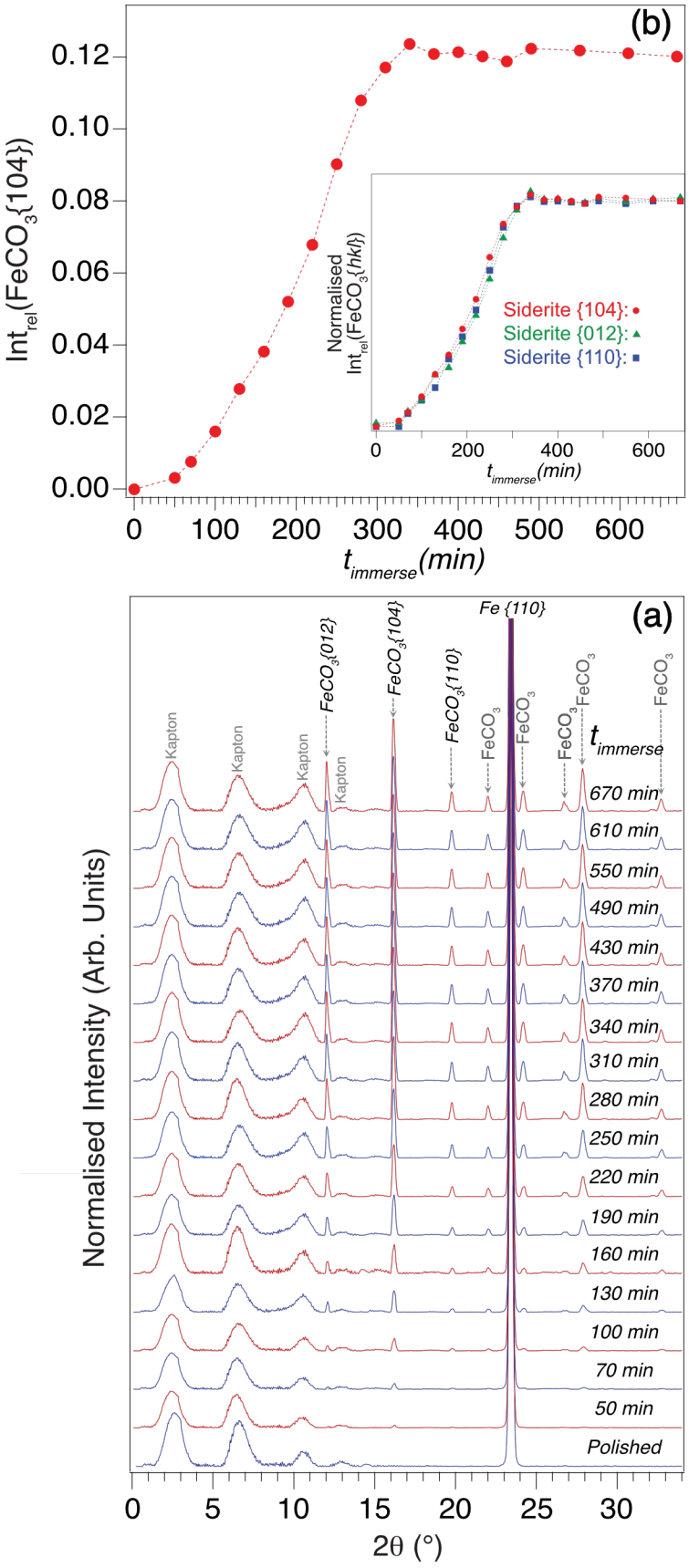
(b)
0.12
0.10
0.08
0.06
0.04
0.02
0.00
Int_rel(FeCO3{104})
0
100
200
300
400
500
600
t_immerse(min)
Normalised Int_rel(FeCO3{hkl})
Siderite {104}:
Siderite {012}:
Siderite {110}:
0
200
400
600
t_immerse(min)
(a)
Kapton
Kapton
Kapton
Kapton
FeCO3{012}
FeCO3{104}
FeCO3{110}
FeCO3
Fe {110}
FeCO3
FeCO3
FeCO3
FeCO3
t_immerse
670 min
610 min
550 min
490 min
430 min
370 min
340 min
310 min
280 min
250 min
220 min
190 min
160 min
130 min
100 min
70 min
50 min
Polished
Normalised Intensity (Arb. Units)
0
5
10
15
20
25
30
2θ (°)

Figure 2

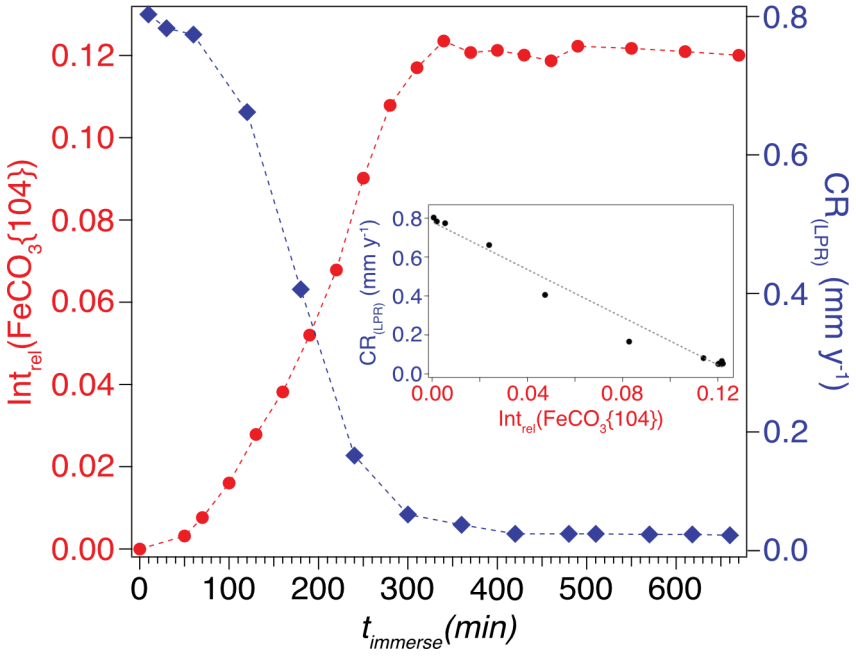
0.12
0.10
0.08
0.06
0.04
0.02
0.00
Int_rel(FeCO3{104})
0.8
0.6
0.4
0.2
0.0
CR(LPR) (mm y-1)
0
100
200
300
400
500
600
t_immerse (min)
0.8
0.6
0.4
0.2
0.0
CR(LPR) (mm y-1)
0.00
0.04
0.08
0.12
Int_rel(FeCO3{104})

Figure 3

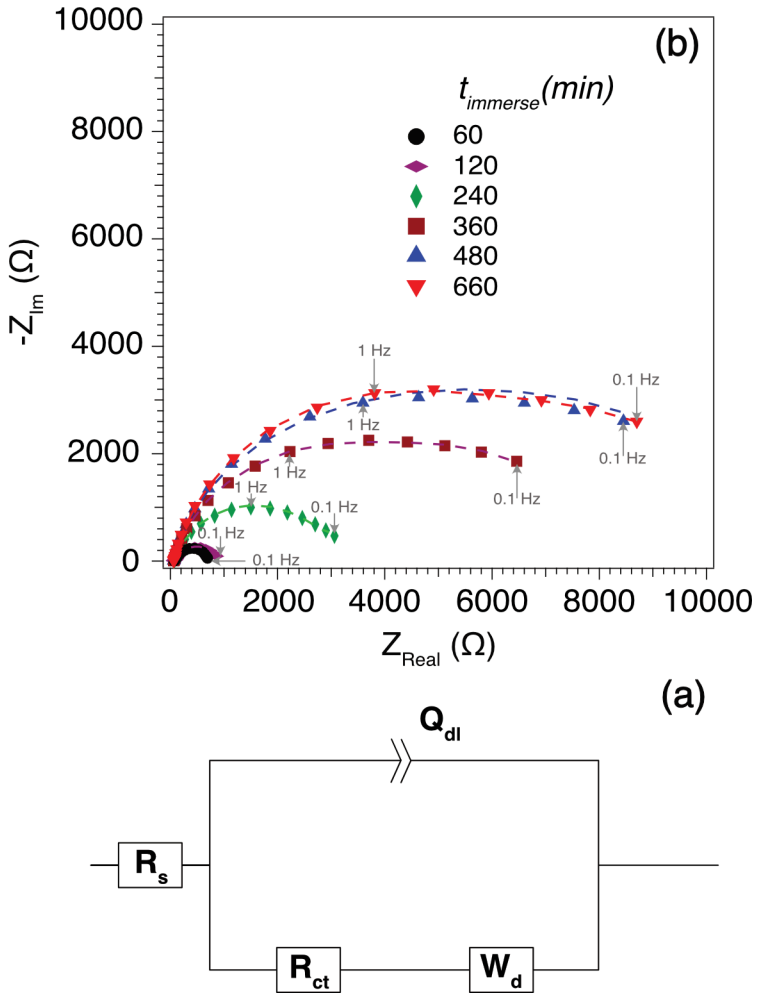
(b)
$t_{immerse}$(min)
60
120
240
360
480
660
-Z_{Im} (Ω)
Z_{Real} (Ω)
1 Hz
0.1 Hz
(a)
Q_{dl}
R_s
R_{ct}
W_d

Figure 4

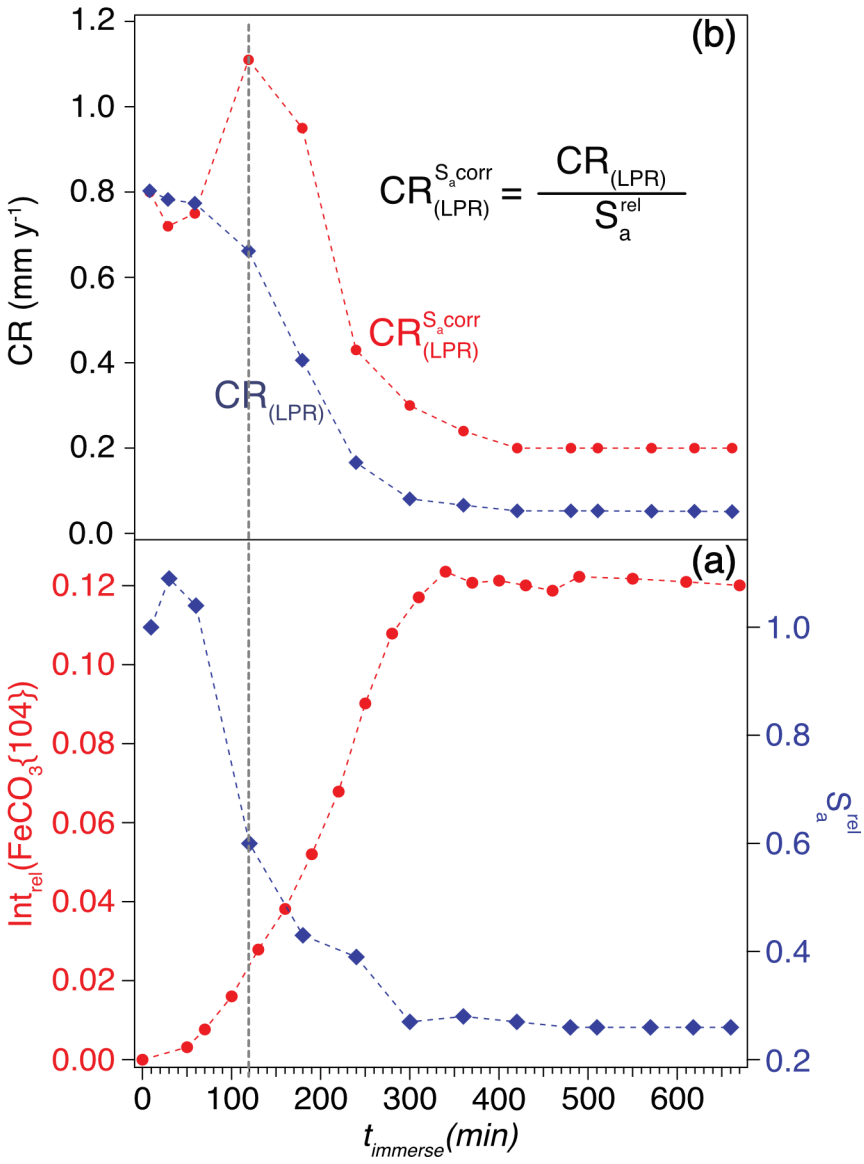
(b)
(a)
CR (mm y-1)
$CR^{S_a corr}_{(LPR)} = \frac{CR_{(LPR)}}{S_a^{rel}}$
$CR^{S_a corr}_{(LPR)}$
$CR_{(LPR)}$
$Int_{rel}(FeCO_3\{104\})$
S_a^{rel}
$t_{immerse}(min)$

Figure 5

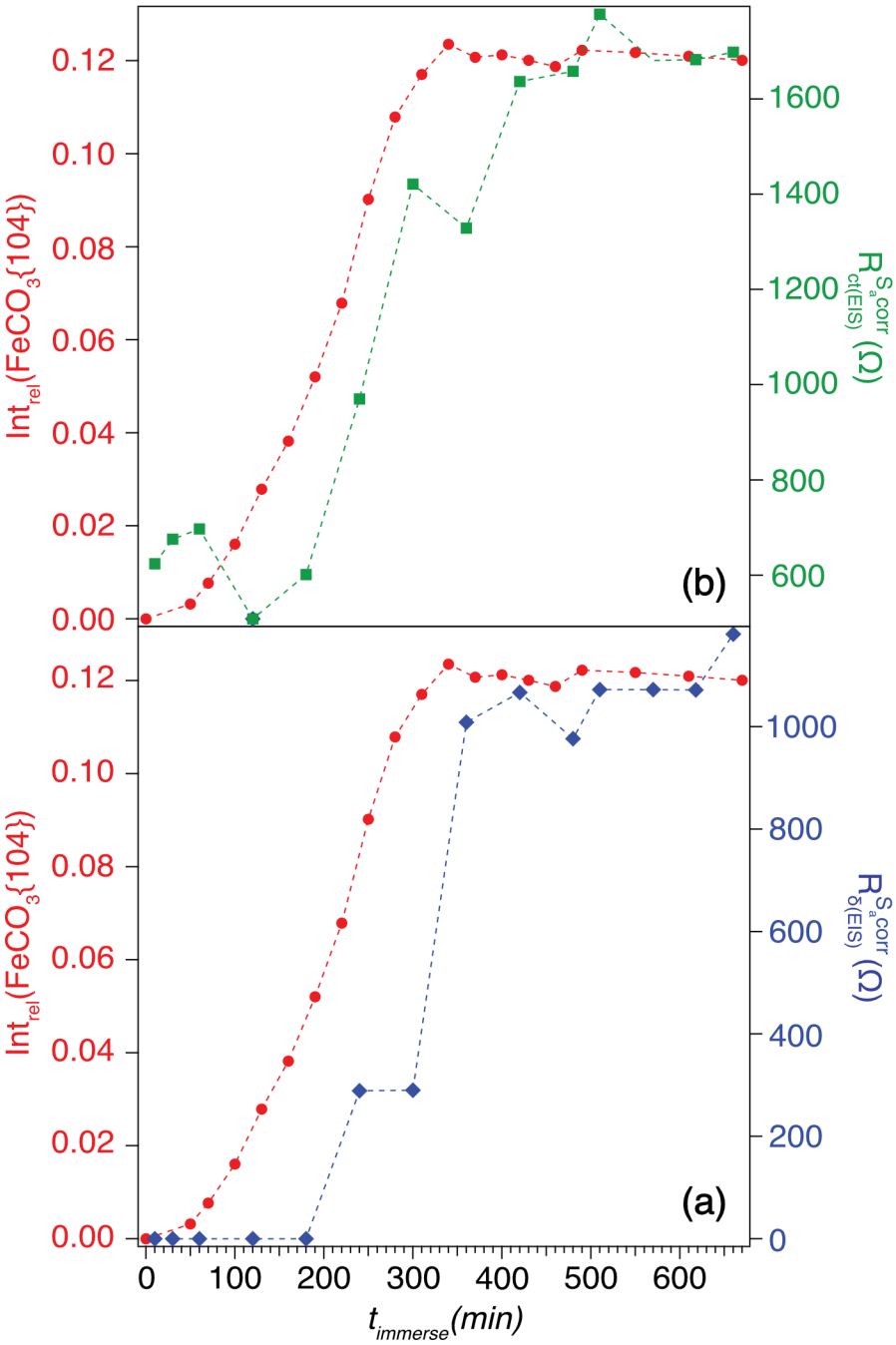
0.12
0.10
0.08
0.06
0.04
0.02
0.00
Int_rel(FeCO3{104})
1600
1400
1200
1000
800
600
R^Sa corr ct(EIS) (Ω)
(b)
0.12
0.10
0.08
0.06
0.04
0.02
0.00
Int_rel(FeCO3{104})
1000
800
600
400
200
0
R^Sa corr δ(EIS) (Ω)
(a)
0
100
200
300
400
500
600
t_immerse(min)

Figure 6

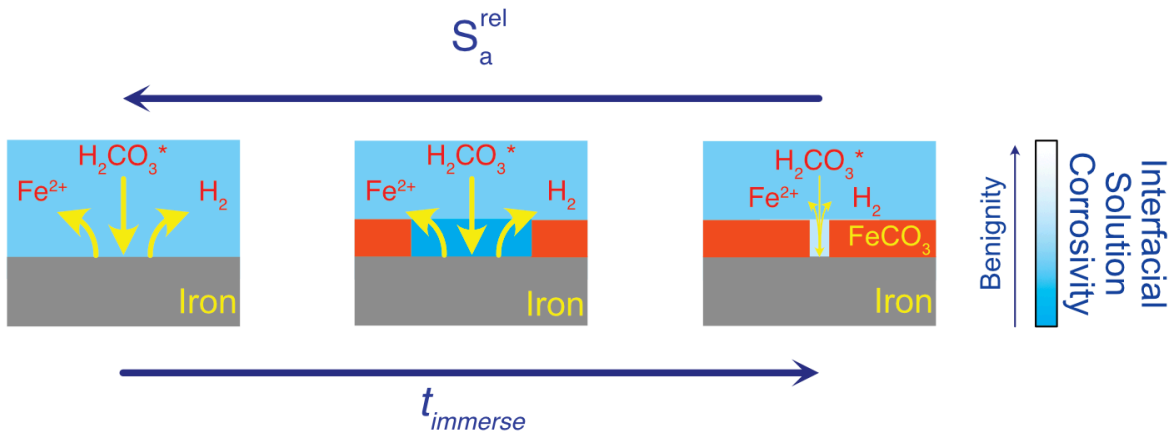
S_a^{rel}
$H_2CO_3^*$
Fe^{2+}
H_2
Iron
$H_2CO_3^*$
Fe^{2+}
H_2
Iron
$H_2CO_3^*$
Fe^{2+}
H_2
$FeCO_3$
Iron
Benignity
Interfacial Solution Corrosivity
$t_{immerse}$

Figure 7

TOC Graphic:

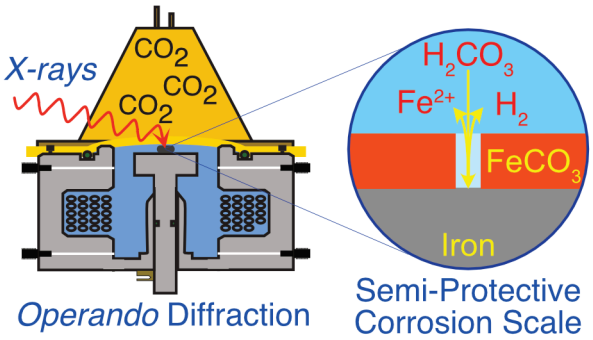
X-rays
CO2
CO2
CO2
Operando Diffraction
H2CO3
Fe2+
H2
FeCO3
Iron
Semi-Protective
Corrosion Scale